

Deep Learning Extraction of the Temperature-Dependent Parameters of Bulk Defects

Yoann Buratti,* Josef Dick, Quoc Le Gia, and Ziv Hameiri



Cite This: *ACS Appl. Mater. Interfaces* 2022, 14, 48647–48657



Read Online

ACCESS |

Metrics & More

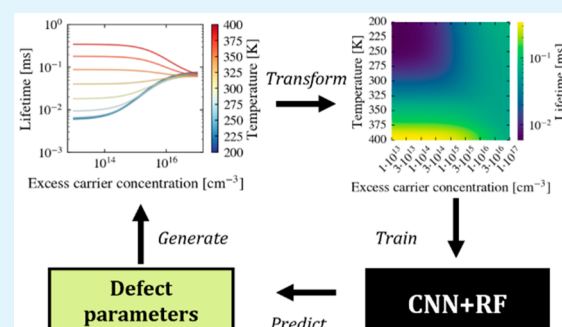
Article Recommendations

ABSTRACT: Bulk defects in silicon solar cells are a key contributor to loss of efficiency. To detect and identify those defects, temperature- and injection-dependent lifetime spectroscopy is usually used, and the defect parameters are traditionally extracted using fitting methods to the Shockley–Read–Hall recombination statistics. In this study, we propose a deep learning-based extraction technique that is based on an alternative representation of the lifetime curves: lifetime mapping in the temperature and minority carrier concentration space. The deep learning approach successfully predicts all the defect parameters while addressing one of the main limitations of the traditional approach of locating the defect in the energy spectrum, which usually outputs two possible solutions. Furthermore, the approach is applied to temperature-dependent defect parameters where the traditional approach is not applicable, achieving satisfying levels of prediction of the defect parameters. Image representation and deep learning have the potential to bolster solar cell characterization techniques by extracting more insights from the characterization data.

KEYWORDS: silicon, solar cells, machine learning, Shockley–Read–Hall, convolutional neural networks, characterization

INTRODUCTION

Photovoltaics (PV) is a key renewable energy technology for enabling a carbon-free society. Almost a third of the planet's renewable energy needs to be produced by PV to limit the rise in global temperatures, according to the intergovernmental panel on climate change (IPCC).¹ To meet the IPCC's targets, improving the efficiency and reliability of PV modules and cells—mostly based on silicon (Si) technology²—is critical. A key contributor to efficiency loss and reliability issues in Si solar cells has been shown to be related to bulk defects.³ Bulk defects originated from the growth method of the silicon ingot and contamination during the manufacturing process.³ It is crucial to characterize and identify those defects to reduce or eliminate their detrimental impact on the efficiency and reliability of PV cells and modules. Bulk defects are well described by the Shockley, Read,⁴ and Hall⁵ (SRH) statistics by three parameters: its energy level E_t and its electron and hole capture cross sections, σ_n and σ_p , respectively. Often, the capture cross-section ratio k (σ_n/σ_p) is used to replace σ_n and σ_p . Using the temperature- and injection-dependent lifetime spectroscopy (TIDLS),^{6,7} the defect parameters can be extracted using the defect parameter solution surface (DPSS) analytical method that was introduced by Rein et al.⁸ This method has been employed to extract the defect parameters of copper,⁹ iron,^{10,11} chromium, aluminum,¹² and many more contaminants.^{7,13–17} The method is based on plotting the best



fit provided by the SRH equation for each lifetime measurement (hence, at each measured temperature). The resulting graph summarizes all the (E_t, k) combinations that provide a good fit. Note that at each temperature an infinite number of (E_t, k) combinations provide good and identical fit quality.^{8,18} All these combinations create the “solution surface” or “DPSS curve”. Repeating this procedure for each measured temperature provides a set of DPSS curves. The true defect parameter lies at the intersection of all these curves. Due to the presence of noise in TIDLS measurements, at least two potential solutions are commonly identified (usually one in the upper half bandgap and one in the lower half bandgap).^{7,13,15} The DPSS method, referred to as the “traditional” approach, has been refined over the years: linearization of the SRH equation under specific conditions has been proposed to facilitate the fitting procedure;^{14,19} faster convergence techniques, such as the Newton–Raphson method, have been adapted;²⁰ and defect parameter contour mapping was developed to visualize the potential solutions.²¹ Recently, a machine learning (ML)

Received: July 28, 2022

Accepted: October 11, 2022

Published: October 19, 2022



based framework was introduced to analyze TIDLS measurements.^{22,23} Multiple ML algorithms were trained to successfully predict the defect parameters (regression) and the half-bandgap location (classification). The method was validated with experimental results, where the parameters obtained by the ML-based and DPSS approaches were shown to agree within an acceptable uncertainty range.²² ML-based regression methods for solar cell parameters to evaluate the impact of the thickness of different layers on the efficiency,^{24,25} understand material properties,^{26,27} and understand current–voltage curve analysis^{12,28–31} were recently published. Regression tasks have also been performed on luminescence images.^{32,33} Classification methods have mainly revolved around automated image analysis using deep learning algorithms such as convolutional neural networks (CNNs),³⁴ where the objective is to classify defects^{35–37} or identify their position in luminescence images.^{38–42}

In this study, we propose to apply deep learning to the defect parameter extraction task. As CNN algorithms excel in performing tasks on images, a new representation of TIDLS measurements is proposed. Instead of the traditional lifetime as a function of the minority excess carrier concentration plot for each measured temperature, we suggest plotting the data as temperature vs minority carrier concentration and mapping the lifetime on a third axis represented with a color gradient. This results in temperature and injection lifetime maps that are then converted into images to be used for CNN training. The new method is also applied for defects with temperature-dependent σ_n and σ_p ,⁴³ which the traditional DPSS approach is unable to solve, as temperature independence is a key assumption of the DPSS approach. The deep learning method is employed to identify the “mode” of temperature dependence (three modes are explored in this study) and consequently predicts the relevant defect parameters for that mode.

Deep learning applied to image representation of characterization data has the potential to extract more insights from the same data than ML-based and traditional methods, and this idea can be applied across multiple characterization techniques and multiple solar cell technologies such as perovskites, thin films, and tandems.

METHODOLOGY

The impact of a defect on the minority carrier lifetime is determined using the SRH recombination statistics:^{4,5}

$$\tau_{SRH} = \frac{\tau_{p0} \cdot (n_0 + n_1 + \Delta n) + \tau_{n0} \cdot (p_0 + p_1 + \Delta n)}{n_0 + p_0 + \Delta n} \quad (1)$$

with

$$\tau_{p0} = (\sigma_p \cdot v_p \cdot N_t)^{-1} \quad (2)$$

$$\tau_{n0} = (\sigma_n \cdot v_n \cdot N_t)^{-1} \quad (3)$$

$$n_1 = n_i \cdot e^{E_t / k_B T} \quad (4)$$

$$p_1 = n_i \cdot e^{-E_t / k_B T} \quad (5)$$

where τ_{SRH} is the SRH lifetime; n_0 (p_0) is the electron (hole) carrier concentration at thermal equilibrium; Δn is the excess minority carrier concentration; v_n (v_p) is the electron (hole) thermal velocity calculated using the model of Green et al.;⁴⁴ N_t is the defect density; n_i is the intrinsic carrier concentration calculated using the model of Couderc et al.,⁴⁵ considering

bandgap narrowing from the model of Yan et al.;⁴⁶ k_B is Boltzmann's constant; and T is the temperature. E_t is defined relative to the intrinsic energy of Si ($E_t = 0$ eV is at midgap) and grows positive as E_t gets closer to the conduction band. The n_1 and p_1 terms govern how the defect energy level E_t impacts the SRH lifetime. As discussed, often k is used as an alternate defect parameter:

$$k := \frac{\sigma_n}{\sigma_p} = \frac{v_p \cdot \tau_{p0}}{v_n \cdot \tau_{n0}} \quad (6)$$

which is usually reported alongside E_t in the literature.^{7,8,10–17}

In the SRH equation (eq 1), most terms have a temperature dependency (thermal velocities, thermal equilibrium carrier concentration, and intrinsic carrier concentration); however, the defect parameters are usually assumed to be independent of temperature.^{8,14} Although this assumption simplifies the defect parameter extraction, it is not valid for many defects.⁴³ In particular, two main temperature-dependent capture mechanisms have been identified: (i) multiphonon emission capture⁴⁷ and (ii) cascade capture.⁴⁸ Each of these capture mechanisms results in a different parametrization of the capture cross-section relative to the temperature. Capture cross-sections following a multiphonon emission capture mechanism increase with increasing temperature following a Boltzmann exponential law:^{43,47}

$$\sigma(T) = \sigma_0 \cdot e^{-E_\infty \cdot \left(\frac{1}{k_B T} - \frac{1}{k_B T_0} \right)} \quad (7)$$

while those following a cascade capture mechanism decrease with increasing temperature following a power law:^{43,48}

$$\sigma(T) = \sigma_0 \cdot \left(\frac{T_0}{T} \right)^\alpha \quad (8)$$

with σ_0 being the capture cross-section at temperature T_0 , E_∞ the activation energy, and α the power law coefficient. Each capture mode can be defined for either σ_n or σ_p , and the corresponding subscript will be applied to the capture parameter ($E_{\infty,n}$, $E_{\infty,p}$, α_n , α_p). Here, we also denote k_0 as the capture cross-section ratio at T_0 .

When measuring the SRH lifetime curves through TIDLS, measurement noise impacts the extraction of the defect parameters, usually by impacting the DPSS resolution, leading to uncertainties in predicting the defect parameters. As discussed, in the DPSS approach, noise often results in uncertainty as to whether the defect energy level is in the upper bandgap half ($E_t > 0$ eV) or lower bandgap half ($E_t < 0$ eV).^{7,8,13,14} To mimic the noise seen in measurements, a Gaussian noise that scales inversely proportional to Δn (low Δn have higher noise) can be added to the lifetime:

$$\tau_{SRH,noise}(\Delta n) = \tau_{SRH}(\Delta n) \cdot \left(1 + \mathcal{N}(0, \epsilon_n^2) \cdot \ln \left(\frac{\Delta_0}{\Delta n} \right) \right) \quad (9)$$

where the noise is drawn from a normal distribution $\mathcal{N}(0, \epsilon_n^2)$ for each Δn point (ϵ_n is the noise scale parameter) before being scaled by the logarithmic factor, and Δ_0 is the excess minority carrier concentration with zero noise. At $\Delta n = \Delta_0$, the logarithmic factor becomes 0, and the SRH lifetime has no added noise. The noise modeling and the scale of ϵ_n are motivated by experimental observations of TIDLS measurements. Each lifetime curve has unique noise, but the noise

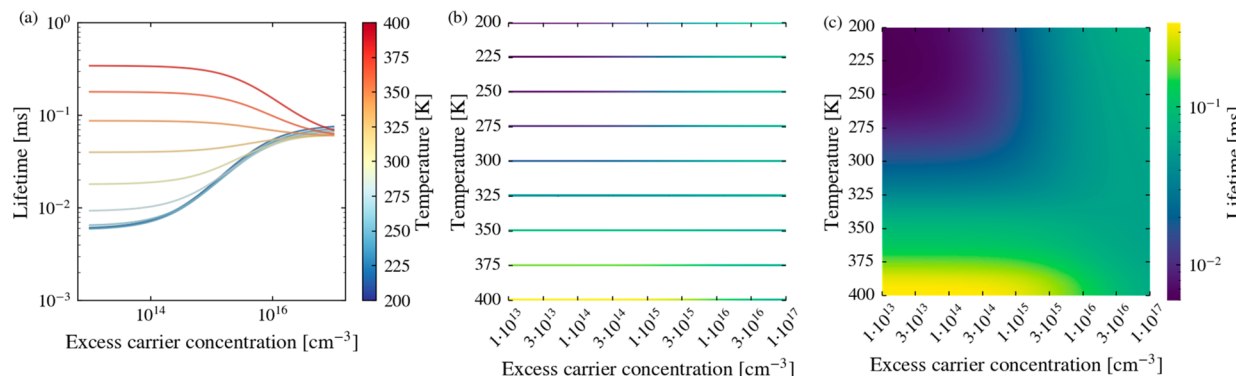


Figure 1. (a) Traditional SRH lifetime curves represent a defect ($E_t = 0.03$ eV; $k = 10$) across nine temperatures, (b) the rearranged SRH lifetime curves in the temperature and injection space, and (c) the temperature and injection lifetime maps after rescaling and interpolation.

generation parameters are kept constant across all the curves for consistency.

SRH lifetime curves are presented as lifetime as a function of Δn for one (IDLS)^{8,49} or multiple (TIDLS)^{7,13,15} temperatures. In this paper, we present an alternative method to present the lifetime: using temperature and injection lifetime maps (TILMs). An example of the SRH lifetime curves of a defect ($E_t = 0.03$ eV; $k = 10$) is shown in Figure 1(a) for nine temperatures (linearly spread) across 100 excess carrier concentrations (logarithmically spread). The SRH curves are rearranged by presenting the lifetime using a third axis (a color gradient) as a function of the temperature (y-axis) and Δn (x-axis) as shown in Figure 1(b). The TILM is converted via interpolation⁵⁰ to a 224 × 224 pixel image, where the choice of the TILM image size is determined by the choice of the deep learning algorithm but can be adapted to any required size. Different regions can be identified in the TILM image: high lifetime (yellow) for high temperatures and low-to-mid injection levels, low lifetime (dark blue) for low temperature and low injection levels, and midlifetime (green) for high injection levels across all temperatures, which is consistent with the SRH lifetime curves. Compared to the SRH lifetime curves, the TILM image can provide a clearer snapshot of the defect's impact on the lifetime across multiple temperatures and injection levels, with the different high and low lifetime regions easily identifiable. Furthermore, having access to a data set of images (TILM) enables the use of powerful deep learning techniques such as CNNs.

Similarly to our previous study on defect parameter extraction using ML (DPML),²² multiple random combinations of defect parameters have been used to generate a data set of millions of lifetime curves. For each defect parameter combination, nine temperatures and 100 excess carrier concentrations are used to generate the lifetime data. The simulation parameters' values and ranges are given in Table 1. Individual data sets are generated for each of the applications that are discussed in the results section: 100 000 defects for the temperature independence application and 300 000 defects for the temperature dependence application.

The generated curves are converted into TILM images as discussed above. The images are then used to train a CNN (based on a VGG network⁵¹) to classify the defect energy level into the correct half-bandgap (upper: $E_t > 0$ eV or lower: $E_t < 0$ eV) or to determine the temperature dependence capture mode (radiative, multiphonon emission, or cascade capture), depending on the application. The CNN is composed of

Table 1. SRH Lifetime Curve Dataset Simulation Parameter Range

Parameter	Symbol	Range or value	Unit
Defect energy level	E_t	[−0.55; 0.55]	eV
Capture cross-sections	σ_n, σ_p	[10^{-17} ; 10^{-13}]	cm ²
Capture cross-section ratio	k	[10^{-4} ; 10^4]	—
Excess carrier concentration	Δn	[10^{13} ; 10^{17}]	cm ⁻³
Temperature	T	[200, 400]	K
Defect density	N_t	10^{12}	cm ⁻³
Doping density	N_{dop}	5.1×10^{15}	cm ⁻³
Doping type	-	{p}	—
Power law coefficient for cascade capture	α	[1.1; 4]	—
Activation energy for multiphonon emission capture	E_∞	[0.01; 0.25]	eV
Noise scale parameter	ϵ_n	0.01	—
Excess carrier concentration with zero noise	Δ_0	10^{17}	cm ⁻³

“feature extraction” block (convolutional and pooling layers) and a “classification” block (fully connected layers).³⁴ After the CNN training, the “classification” block is discarded, and the weights of the “feature extraction” block are fixed. Hence, we use the CNN as a feature extractor, transforming the TILM image into a condensed feature vector (from a 224 × 224 pixel image into a 2048 point vector). The resulting set of deep learning features is then used to train a random forest (RF)⁵² algorithm to predict the defect parameters ($E_{t,+}, E_{t,-}, k$) and the relevant capture mode parameters ($E_{\infty,n}, E_{\infty,p}, \alpha_n, \alpha_p$). We named this method “DPDL” (defect parameter deep learning extraction). A summary of the training and prediction framework for DPDL is shown in Figure 2. Compared to the DPML approach which uses the vectorized form of the lifetime curves directly to train the RF, the CNN approach imbues its learning of the classification task prediction into the extracted features before training the RF for the regression tasks. The DPDL approach consists of CNN for classification and CNN + RF for regression, while the DPML uses RF for both classification and regression tasks.

The CNN and RF are trained on 90% of the generated data set and evaluated on the remaining 10%. To evaluate the ML algorithms on the regression tasks, the coefficient of determination (R^2) and the root-mean-square error (RMSE) are used:⁵³

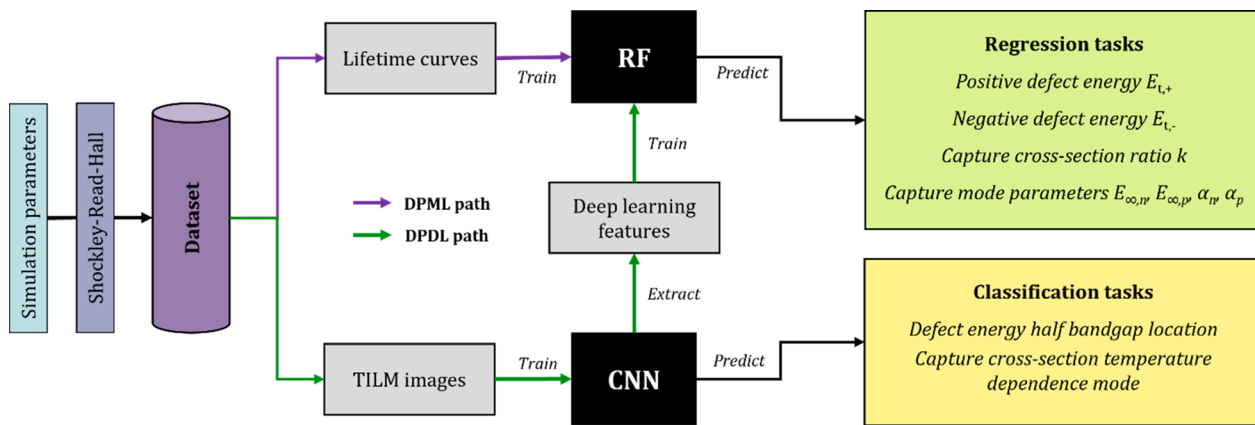


Figure 2. Deep learning framework for defect parameter extraction. A set of randomly selected defect parameters are used to generate a large data set through the SRH recombination statistics. The CNN is trained first for classification tasks using the TILM images before being used as a feature extractor to train an RF for the regression tasks.

$$R^2 := 1 - \frac{\sum_{i=1}^N (y_i - \hat{y}_i)^2}{\sum_{i=1}^N (y_i - \bar{y})^2} \quad (10)$$

$$\text{RMSE} := \sqrt{\frac{1}{N} \sum_{i=1}^N (y_i - \hat{y}_i)^2} \quad (11)$$

where y_i , \hat{y}_i , and \bar{y} are, respectively, the true and predicted defect parameter of defect i and the average value of the defect parameter in the data set of size N . For the classification task, the CNNs are trained over 50 epochs and evaluated using the cross-entropy loss (CEL) metric, defined as³⁴

$$\text{CEL} := \sum_{i=1}^N \left(- \sum_{c=1}^M b_{i,c} \log p_{i,c} \right) \quad (12)$$

where M is the number of classes; $b_{i,c}$ is the binary indicator (0 or 1) of defect i in class c ; and $p_{i,c}$ is the predicted probability that defect i is in class c . A perfect model would have a CEL of 0. The classification tasks are also evaluated through confusion matrices and their associated metrics such as accuracy, precision, recall, and F_1 score.⁵⁴ The ML methods are implemented using Python, with the packages Scikit-learn⁵⁵ and Pytorch.⁵⁶ More details on the structure and hyperparameters of the ML and CNNs used can be found in the provided GitHub link in the data and code availability section. The computer used for training has an Intel Xeon W-2145 processor, a central processing unit of up to 3.70 GHz, and a random-access memory of 64 GB. An NVIDIA Titan V Graphical Processing Unit (GPU) is used for training the deep learning models.

■ DEEP LEARNING DEFECT PARAMETER EXTRACTION

We first investigate the performance of the proposed method for the temperature-independent case. We also compare the performance of the DPDL with the performance of the DPML. A data set of 100 000 unique combinations of defect parameters is generated and used to evaluate the classification of the energy level half-bandgap location (binary classification). The resulting confusion matrix of the validation set is shown in Figure 3(a). The CNN achieved an accuracy of 90.0%. For comparison, an NN classifier trained on the same

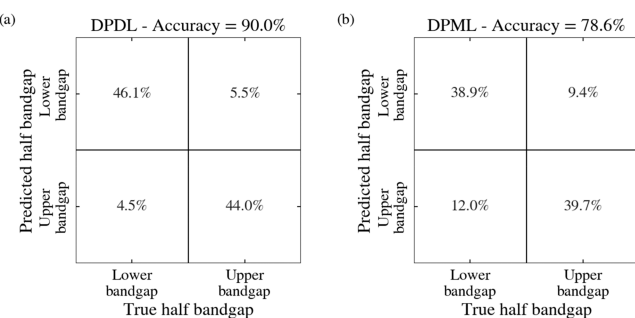


Figure 3. True vs predicted half bandgap location of the E_t confusion matrix on the validation data set for (a) a CNN trained on TILM images (DPDL) and (b) an NN trained on the vectorized SRH lifetime curves (DPML).

set using the DPML methodology achieved an accuracy of only 78.6% [Figure 3(b)]. Hence, the DPDL approach outperformed the DPML. Deep learning combined with our proposed image representation significantly improved the detection accuracy between the two half bandgaps. We assume that the more complex models of the CNN and the access to the TILM image representation significantly improve the performance of the model.

The regression task results are presented in Figure 4, where the predicted and true defect parameter predictions are shown for DPDL [Figure 4(a,b)] and DPML [Figure 4(c,d)]. For each graph, the scoring metrics (R^2 and RMSE) are shown. For the prediction of E_t , two regressors are trained on each half-bandgap ($E_{t,+}$ and $E_{t,-}$) and are presented together in Figure 4(a,c). For the k predictions, the RF is trained and evaluated into predicting the \log_{10} of k . Since k spans multiple orders of magnitude, this is to ensure that scoring metrics such as the RMSE are still meaningful and not biased to the higher orders of magnitude.

The DPDL approach achieves an RMSE of 0.009 eV and an R^2 of 0.999 for E_t [Figure 4(a)] and an RMSE of 0.030 and R^2 of 0.999 for $\log_{10}(k)$ [Figure 4(b)]. With the half-bandgap location prediction accuracy of 90% [Figure 3(a)], the DPDL approach completely solves the extraction of temperature-independent defect parameters. For comparison, the DPML approach has also been trained on the same data set, achieving an RMSE of 0.013 eV for E_t [Figure 4(c)] and an RMSE of 0.034 for $\log_{10}(k)$ [Figure 4(d)], matching previously observed

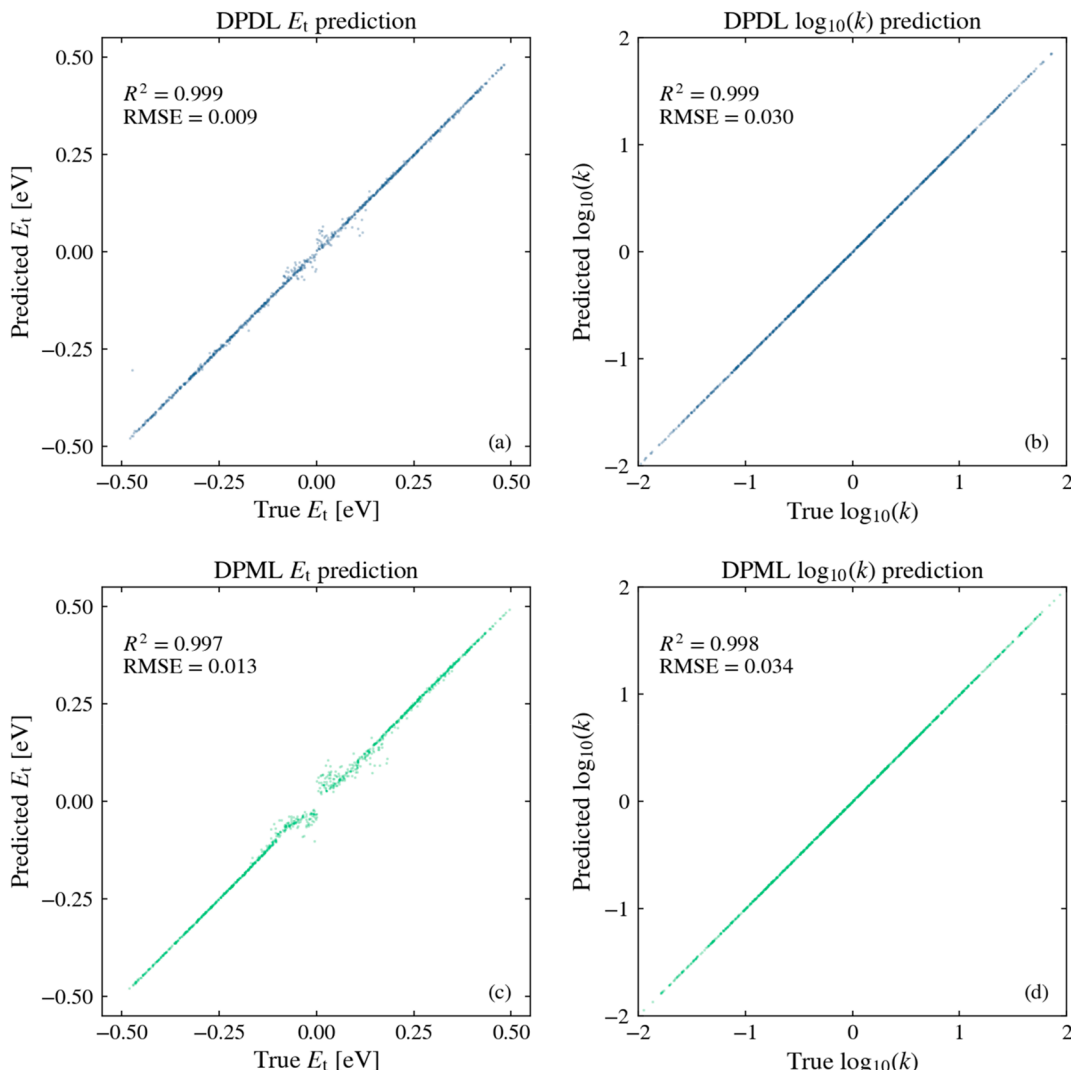


Figure 4. True vs predicted E_t and $\log_{10}(k)$ on the validation data set for both (a,b) the DPDL and (c,d) the DPML approaches.

results.²² In particular, the DPML approach has difficulties predicting near the midgap ($E_t \sim 0$ eV) due to the negligible dependency of the SRH equation [eq 1] in E_t when E_t is near 0 eV.²² However, the DPDL surmounts that issue with better prediction near the midgap, explaining the overall better E_t RMSE. This is a remarkable achievement as it has been shown that in many cases the differences in the lifetime curves when defects are located near the midgap can be below 50 ns.²² As the CNN is trained on the half-bandgap location classification task and therefore extracts features principally related to E_b , an improvement in E_t prediction is expected for the DPDL, while k predictions are not expected to improve. However, it is notable that even with an E_t -focused feature extraction the DPDL manages to match the DPML's performance in predicting k .

To compare the DPDL and DPML to the traditional DPSS method, lifetime curves of a defect ($E_t = -0.37$ eV; $k = 0.25$), without and with added noise, have been generated. The defect parameters are then extracted using the different methods. Figure 5 presents the lifetime curves of that defect without [Figures 5(a,c,e,g)] and with [Figures 5(b,d,f,h)] noise. The SRH lifetime curves are shown in Figure 5(a,b). As seen in experimental measurements,⁸ the noise strongly impacts the low injection levels, resulting in some overlap of the SRH

lifetime curves, especially at low temperatures (blue–yellow curves). The effect is similar in the TILM images [Figure 5(c,d)]; however, the different regions (high lifetime in yellow and low lifetime in dark blue) are still easily recognizable, helping the CNN to extract the relevant features. For the DPSS approach, the DPSS curves are first calculated using the SRH lifetime curves^{8,14,19} and then plotted for each temperature [Figures 5(e,f)]. As discussed, each DPSS curve represents the set of (E_b , k) that best fits the SRH equation. There is an infinite number of potentials (E_b , k) per temperature, and the DPSS prediction lies at the intersection of all the DPSS curves. As can be seen in Figure 5(e,f), the DPSS method identifies two potential intersection points, one in the upper half-bandgap and one in the lower half-bandgap. The sharpness of the intersections is quantified as the standard deviation of the DPSS curves over the mean of the DPSS curves as shown in Figure 5(g,h). The sharpness is only defined where all the DPSS curves exist (hence the discontinuous shape of the curves) and the minimum sharpness points toward the best intersection. In the case without noise [Figure 5(g)], the lower half-bandgap intersection point is the sharpest. From the sharpness minima, the value of E_t can be found, and by reporting E_t on the DPSS curves, the value of k can be identified. However, with noise [Figure 5(h)], the sharper

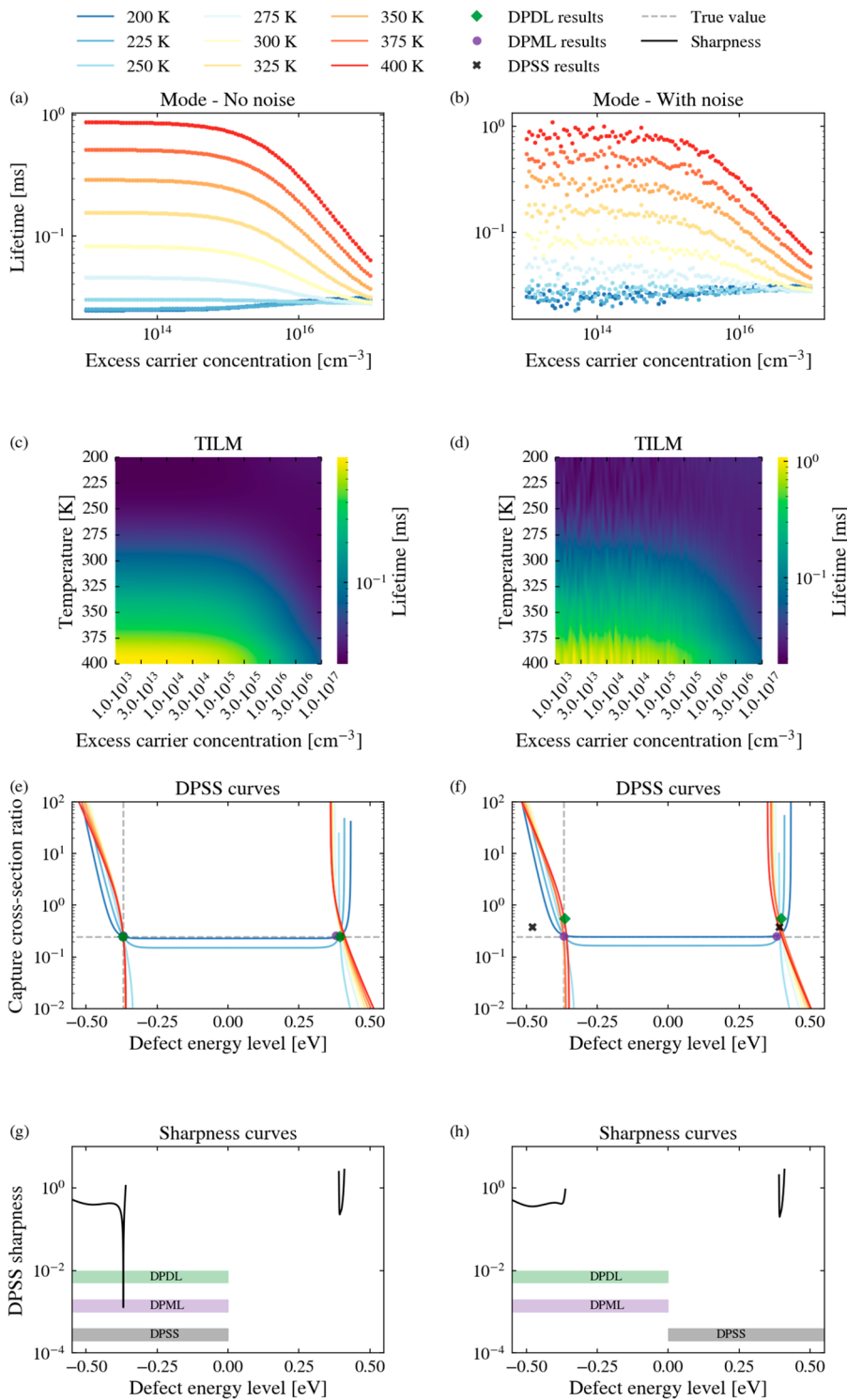


Figure 5. Simulated defect ($E_t = -0.37$ eV; $k = 0.25$) (a,b) SRH lifetime curves, (c,d) TILM images, (e,f) calculated DPSS curves, and (g,h) DPSS sharpness curves for both (a,c,e,g) without and (b,d,f,h) with added noise.

minimum is in the upper half-bandgap; thus, the DPSS method predicts the incorrect half-bandgap and therefore an incorrect E_v . In the sharpness graphs [Figures 5(g,h)], the prediction of the half-bandgap classification tasks by each method is represented by a colored band in the corresponding half. While the DPSS makes an erroneous prediction, both the DPML and DPDL predict the correct half-bandgap in both cases, with and without added noise. For each method, the (E_v , k) prediction in each bandgap half is shown over the DPSS

curves [Figure 5(e,f)] as symbols (DPDL – green diamond; DPML – purple circle; DPSS – black cross); the true value of the defect parameters is also shown as the intersection of the dotted gray line. Without added noise [Figure 5(e)], all methods predict the correct (E_v , k) values; however, with added noise [Figure 5(f)] the DPDL and DPML prediction has the correct E_v , but DPDL has an incorrect k value. As discussed previously in Figure 4, the DPDL focuses on features related to E_t rather than k , which seems to be accentuated by

the presence of noise. Both DPML and DPDL perform better than DPSS with added noise, highlighting the general robustness to noise of ML-based methods.

Figure 6 compares the errors in predicting the defect parameters using a set of 1000 defects with and without noise

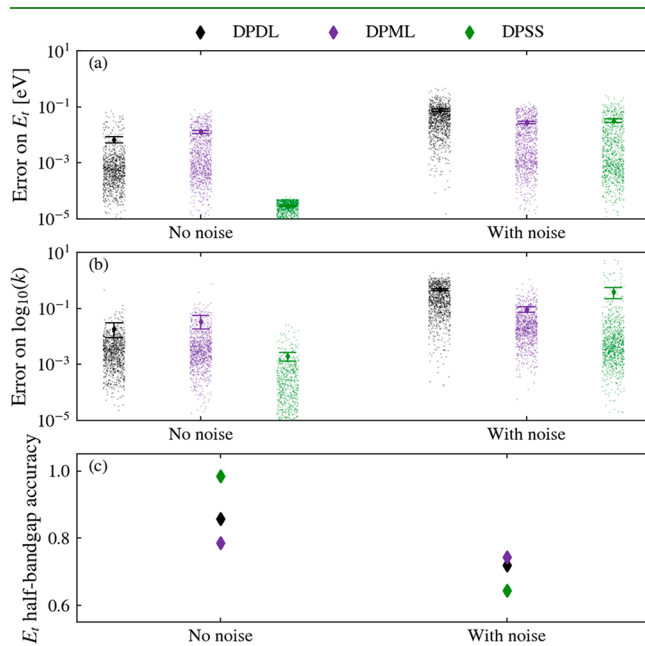


Figure 6. Error comparison over a set of 1000 defects for predictions of (a) E_t , (b) k , and (c) half-bandgap accuracies of the different parameter extraction methods: DPDL – green, DPML – purple, and DPSS – black.

(separate from the training sets) for each of the methods (DPDL, DPML, and DPSS). For the defect parameters (E_t and k), the error is shown as an absolute error [Figure 6(a,b)] on a log scale. The RMSE of each distribution (diamond) with its 95% confidence interval (error bar) is also shown. For E_t [Figure 6(a)], the correct half-bandgap is assumed when calculating the error, while the accuracy of the half-bandgap prediction is shown over the entire data set in Figure 6(c).

Without added noise, results consistent with Figure 4 are observed, with an RMSE for E_t of 0.007 eV for DPDL, which outperformed the DPML with an RMSE of 0.013 eV. The DPSS prediction being extracted from the sharpness curve is limited by the parametrization step (used to plot the DPSS curves) which is here 0.001 eV. For the prediction of $\log_{10}(k)$, the DPDL performed better (RMSE = 0.018) than DPML (RMSE = 0.034) despite the limitation of the feature extractor of the DPDL being focused on E_t . The DPSS obtained an RMSE of 0.002, which directly comes from the parametrization step as translated in the k -space from the DPSS curve. For the half-bandgap location prediction, the DPDL performed at 85.8% accuracy, while the DPML only obtained 78.6% accuracy. The DPSS, being a quasi-analytical solution when no noise is present, unsurprisingly reaches 98.4% accuracy. With added noise, the DPDL, with an RMSE of 0.077 eV and 0.47 on the prediction of E_t and $\log_{10}(k)$, respectively, performs slightly worse than the DPML on the regression targets, with an RMSE of 0.028 eV and 0.09, respectively, and at a comparable level to the DPSS with an RMSE of 0.066 eV and 0.45, respectively. As shown in Figure 5, the DPSS performance significantly drops when noise is added. In particular, the half-bandgap location prediction accuracy dropped to 64.4%, barely better than random guessing, while the DPDL and DPML retain a much higher accuracy of 72.0% and 74.3%, respectively. As discussed previously, the DPDL is not specifically calibrated to extract relevant k features and focuses on E_t features. The higher accuracies highlight the superiority of the ML-based methods when noise is present.

Another advantage of ML-based methods is the potential improvement with access to a larger data set or more lifetime curves for each measurement. In practice, a continuous temperature measurement range can be achieved by gradually heating or cooling the sample from room temperature and letting it cool down (or heat up) to room temperature while continuously measuring the lifetime. With access to hundreds of temperature-dependent lifetime curves, the calculation complexity of DPSS is significantly increased, while the DPDL approach stays the same, as the data are converted into the TILM image. The increase in the number of

Table 2. DPDL (Accuracy = 99.0%) and DPML (Accuracy = 96.1%) F_1 Score for the Nine Combinations of Capture Cross-Section Modes^a

Mode abbreviation	Mode σ_n	Mode σ_p	k/k_0	DPDL F_1 score	DPML F_1 score
RAD-RAD	Radiative	Radiative	1	99.6%	96.3%
RAD-MPE	Radiative	Multiphonon Emission	$e^{E_{\infty,p}\left(\frac{1}{k_B T} - \frac{1}{k_B T_0}\right)}$	98.8%	95.1%
RAD-CAS	Radiative	Cascade	$\left(\frac{T}{T_0}\right)^{\alpha_p}$	99.7%	98.5%
MPE-RAD	Multiphonon Emission	Radiative	$e^{-E_{\infty,n}\left(\frac{1}{k_B T} - \frac{1}{k_B T_0}\right)}$	98.3%	95.7%
MPE-MPE	Multiphonon Emission	Multiphonon Emission	$e^{(E_{\infty,p}-E_{\infty,n})\left(\frac{1}{k_B T} - \frac{1}{k_B T_0}\right)}$	98.2%	95.6%
MPE-CAS	Multiphonon Emission	Cascade	$\left(\frac{T}{T_0}\right)^{\alpha_p} \cdot e^{-E_{\infty,n}\left(\frac{1}{k_B T} - \frac{1}{k_B T_0}\right)}$	99.3%	96.8%
CAS-RAD	Cascade	Radiative	$\left(\frac{T}{T_0}\right)^{-\alpha_n}$	98.6%	97.1%
CAS-MPE	Cascade	Multiphonon Emission	$\left(\frac{T}{T_0}\right)^{-\alpha_n} \cdot e^{E_{\infty,p}\left(\frac{1}{k_B T} - \frac{1}{k_B T_0}\right)}$	99.1%	96.6%
CAS-CAS	Cascade	Cascade	$\left(\frac{T}{T_0}\right)^{\alpha_p-\alpha_n}$	99.2%	99.2%

^aFor each combination, the capture cross-section ratio temperature-dependent component and its abbreviation are also shown.

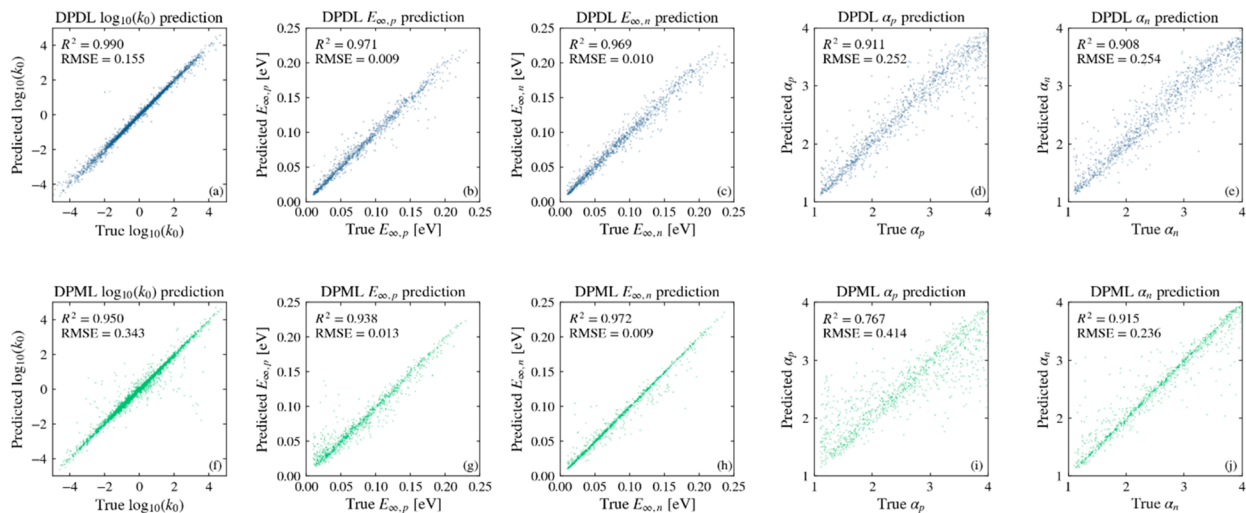


Figure 7. Defect parameter extraction evaluation graphs for the prediction of (a,f) $\log_{10}(k_0)$, (b,g) σ_p multiphonon emission capture ($E_{\infty,p}$), (c,h) σ_n multiphonon emission capture ($E_{\infty,n}$), (d,i) σ_p cascade capture (α_p), and (e,j) σ_n cascade capture (α_n), shown for both (a–e) the DPDL and (f–j) DPML approaches.

temperatures increases the resolution of that image without changing its size. The DPDL approach also provides additional benefits for temperature-dependent parameter extraction.

■ PARAMETER EXTRACTION OF TEMPERATURE-DEPENDENT CAPTURE CROSS-SECTIONS

The DPDL approach is now evaluated using a more complex but realistic model that considers the temperature dependency of the capture cross-section, effectively adding two additional parameters to extract (α or E_∞ for either σ_n or σ_p). Furthermore, an additional classification task is needed to identify the capture mode for each of the capture cross-sections (radiative, multiphonon emission, or capture). Note that these capabilities are outside the limitations of the DPSS method, which cannot extract the parameters of defects with such temperature dependency. The data set used in this section is balanced between the nine possible combinations of temperature-dependent capture modes (see Table 2 for the abbreviation used for each combination). Note that we use the ratio between k and a reference capture cross-section ratio at $T_0 = 300$ K, k_0 . The ratio k/k_0 is derived from eqs 7 and 8 and explicitly shows the dependency in the additional extracted parameters. The regression task for the capture cross-section ratio is shifted from k to k_0 .

As can be seen from Table 2, the DPDL classification task predicts the combination of the capture mode with an overall accuracy of 99.0%. All the F_1 scores of the DPDL are above 98% (ranging from 98.2% to 99.7%), highlighting its outstanding capabilities to obtain information that is outside the abilities of the DPSS approach. To evaluate the performance of the DPML on the same task, an NN classifier is trained on the same data set, and the results are reported in Table 2. The DPML achieves an overall accuracy of 96.1% and F_1 scores ranging from 95.1% to 99.2%. Clearly, the DPDL outperforms the DPML in both average accuracy and F_1 scores in every mode combination. Furthermore, the detection of temperature independence in the defect parameters (RAD-RAD) achieves a near-perfect F_1 score of 99.6%, making the DPDL approach a suitable tool to confirm or deny the

presence of temperature dependency of the capture cross-sections.

For the regression tasks, a regressor is required for k_0 and each of the four capture mode parameters (α_n , α_p , $E_{\infty,n}$, and $E_{\infty,p}$). While the k_0 regressor is trained on the entire data set, the capture mode parameters are trained on the subset where the capture mode is relevant (i.e., the α_n regressor is trained on the combined CAS-RAD, CAS-MPE, and CAS-CAS subsets). The models' performances are evaluated on a testing set (10% of the relevant subset), and each defect parameter's prediction is plotted against its true value in Figure 7, with $\log_{10}(k_0)$ (a,f), $E_{\infty,p}$ (b,g), $E_{\infty,n}$ (c,h), α_p (d,i), and α_n (e,j) for both DPDL (a–e) and DPML (f–j). The DPDL method completely characterizes the temperature-dependent defect with an RMSE of 0.16 for $\log_{10}(k_0)$, 0.01 eV for $E_{\infty,p}$ and $E_{\infty,n}$, and 0.25 for α_p and α_n . All R^2 values are above 0.9, indicating a good correlation between the predicted and true parameter values. For the $E_{\infty,p}$ and $E_{\infty,n}$ [Figure 7(b,c)], the DPDL accurately predicts the activation energy across the entire simulated range, even close to 0 eV where the effects of temperature dependence from multiphonon emission capture are less detectable. The DPML results are shown for comparison. In most cases, the DPDL outperforms the DPML. Notably, the $\log_{10}(k_0)$ DPML's RMSE [Figure 7(f)] is more than double the DPDL's RMSE. Both σ_p mode parameter predictions by the DPML [$E_{\infty,p}$ and α_p ; Figure 7(g,i)] have a lower R^2 and higher RMSE than the DPDL's [Figure 7(b,d)].

The DPDL method shows an excellent capture mode prediction accuracy, k_0 , and capture parameter prediction. The extraction of defect parameters in the presence of such temperature dependence is unachievable by conventional analytical or fitting-based methods, such as the DPSS, while the DPML struggles to predict a subset of the required parameters (α_p for example). As all the main capture cross-section mode combinations are represented, it is not necessary to know the details of the capture mechanism (as predicted by the CNN) to extract the defect parameters. If further prediction accuracy is desired, two improvements to the framework can be undertaken. First, simulating larger data sets will lower the RMSE and increase the R^2 , especially for the

regressor training on subsets of the data (capture parameters). Second, if the capture mechanism is already known, an ML algorithm can be trained on a larger set that is specific to one of the nine capture mode combinations. The temperature-dependent predictions are not expected to match the temperature-independent performance as the problem is more complex. Nonetheless, the results clearly demonstrate the potential of the proposed TILM image representation and the DPDL approach in extracting defect parameters from complex temperature-dependent models.

CONCLUSIONS

In this study, we developed a deep learning-based approach (DPDL) to extract defect parameters from TIDLS measurements. To enable the training of CNNs, a new representation of the TIDLS measurements has been developed, converting the traditional SRH curves into a temperature and injection space, mapping the lifetime across that space. The resulting TILM images are used to train a CNN for different classification tasks and enable ML to use CNN-extracted features for the regression tasks. Additionally, the TILM image representation is useful to quickly grasp the impact of a defect on the bulk lifetime as high or low lifetime regions can easily be identified even in the presence of noise. The main advantage of the DPDL approach is its outstanding capability to successfully extract the temperature-dependent capture cross-sections for a variety of capture mechanisms. These capabilities overcome the most significant limitation of the traditional fitting-based methods (such as the DPSS), their inability to extract the defect parameters when temperature dependence is present. To our knowledge, the developed method is the only method that enables the determination of the capture modes of both the electrons and holes with high accuracy (>99%) and the extraction of the temperature-dependent capture parameters with low RMSE and high R^2 . The deep learning approach enables, for the first time, defect parameter extraction without the need for unrealistic assumptions regarding the temperature dependency of the capture cross-sections. Deep learning and lifetime maps pave the way to parameter extraction for more complex lifetime models, such as multiple defects or two-level defects, and can easily be transferred to other materials, for instance, perovskites, thin films, or tandems, and to other measurement techniques. While a specific physics model would be needed, the proposed machine-learning-based methodology would be identical. Furthermore, the proposed data visualization (TILM) can be replicated for any characterization techniques involving at least independent parameters (injection level and temperature in this study) to allow access to powerful deep learning algorithms.

ASSOCIATED CONTENT

Data Availability Statement

The authors declare that all data and code, including the scripts and model structure, can be found on GitHub [<https://github.com/WhyBeU/DPML>]. Any additional data can be accessed upon request.

AUTHOR INFORMATION

Corresponding Author

Yoann Buratti – UNSW, School of Photovoltaic and Renewable Energy Engineering, Sydney 2052 NSW,

Australia;  orcid.org/0000-0002-3621-9712;
Email: yoann.buratti@gmail.com

Authors

Josef Dick – UNSW, School of Mathematics and Statistics, Sydney 2052 NSW, Australia
Quoc Le Gia – UNSW, School of Mathematics and Statistics, Sydney 2052 NSW, Australia
Ziv Hameiri – UNSW, School of Photovoltaic and Renewable Energy Engineering, Sydney 2052 NSW, Australia;
 orcid.org/0000-0002-2934-4478

Complete contact information is available at:
<https://pubs.acs.org/10.1021/acsami.2c12162>

Author Contributions

Y.B. wrote the simulation and machine learning codes and the initial version of the manuscript. Z.H. supervised the work and contributed to the development of the methodology. Q.L. and J.D. contributed to the development of the methodology.

Notes

The authors declare no competing financial interest.

ACKNOWLEDGMENTS

This work was supported by the Australian Government through the Australian Renewable Energy Agency [ARENA; Projects 2017/RND017 and 2020/RND016]. The views expressed herein are not necessarily the views of the Australian Government, and the Australian Government does not accept responsibility for any information or advice contained herein.

REFERENCES

- (1) Masson-Delmotte, V.; Zhai, P.; Pörtner, H.-O.; Roberts, D.; Skea, J.; Shukla, P. R.; Pirani, A.; Moufouma-Okia, W.; Péan, C.; Pidcock, R.; Connors, S.; Matthews, J. B. R.; Chen, Y.; Zhou, X.; Gomis, M. I.; Lonnoy, E.; Maycock, T.; Tignor, M.; Waterfield, T. *Global Warming of 1.5°C - an IPCC Special Report on the Impacts of Global Warming of 1.5°C above Pre-Industrial Levels and Related Global Greenhouse Gas Emission Pathways, in the Context of Strengthening the Global Response to the Threat of Climate Change, Sustainable Development, and Efforts to Eradicate Poverty*; IPCC: In Press, 2018.
- (2) Green, M. A. Photovoltaic Technology and Visions for the Future. *Prog. Energy* **2019**, *1* (1), 013001.
- (3) Schmidt, J.; Lim, B.; Walter, D.; Bothe, K.; Gatz, S.; Dullweber, T.; Altermatt, P. P. Impurity-Related Limitations of next-Generation Industrial Silicon Solar Cells. In *38th IEEE Photovoltaic Specialists Conference*; 2012; pp 1–5. DOI: [10.1109/PVSC-Vol2.2012.6656779](https://doi.org/10.1109/PVSC-Vol2.2012.6656779).
- (4) Shockley, W.; Read, W. T. Statistics of the Recombinations of Holes and Electrons. *Phys. Rev.* **1952**, *87* (5), 835–842.
- (5) Hall, R. N. Electron-Hole Recombination in Germanium. *Phys. Rev.* **1952**, *87* (2), 387–387.
- (6) Schmidt, J. Temperature- and Injection-Dependent Lifetime Spectroscopy for the Characterization of Defect Centers in Semiconductors. *Appl. Phys. Lett.* **2003**, *82* (13), 2178–2180.
- (7) Zhu, Y.; Rougjeux, F.; Grant, N.; Mullins, J.; De Guzman, J. A.; Murphy, J. D.; Markevich, V. P.; Coletti, G.; Peaker, A. R.; Hameiri, Z. New Insights into the Thermally Activated Defects in N-Type Float-Zone Silicon. *AIP Conf. Proc.* **2019**, *2147* (1), 140014.
- (8) Rein, S. *Lifetime Spectroscopy: A Method of Defect Characterization in Silicon for Photovoltaic Applications*; Springer Science & Business Media, 2005.
- (9) Inglese, A.; Lindroos, J.; Vahlman, H.; Savin, H. Recombination Activity of Light-Activated Copper Defects in p-Type Silicon Studied by Injection- and Temperature-Dependent Lifetime Spectroscopy. *J. Appl. Phys.* **2016**, *120* (12), 125703.
- (10) Birkholz, J. E.; Bothe, K.; Macdonald, D.; Schmidt, J. Electronic Properties of Iron-Boron Pairs in Crystalline Silicon by Temperature-

- and Injection-Level-Dependent Lifetime Measurements. *J. Appl. Phys.* **2005**, *97* (10), 103708.
- (11) Paudyal, B. B.; McIntosh, K. R.; Macdonald, D. H. Temperature Dependent Electron and Hole Capture Cross Sections of Iron-Contaminated Boron-Doped Silicon. In *34th IEEE Photovoltaic Specialists Conference*; 2009; pp 001588–001593. DOI: 10.1109/PVSC.2009.5411380.
- (12) Sun, C.; Rougieroux, F. E.; Degoulange, J.; Einhaus, R.; Macdonald, D. Reassessment of the Recombination Properties of Aluminium–Oxygen Complexes in n- and p-Type Czochralski-Grown Silicon. *Physica Status Solidi B* **2016**, *253* (10), 2079–2084.
- (13) Jafari, S.; Abbott, M.; Zhang, D.; Wu, J.; Jiang, F.; Hameiri, Z. Bulk Defect Characterization in Metalized Solar Cells Using Temperature-Dependent Suns-Voc Measurements. *Sol. Energy Mater. Sol. Cells* **2022**, *236*, 111530.
- (14) Murphy, J. D.; Bothe, K.; Krain, R.; Voronkov, V. V.; Falster, R. J. Parameterisation of Injection-Dependent Lifetime Measurements in Semiconductors in Terms of Shockley-Read-Hall Statistics: An Application to Oxide Precipitates in Silicon. *J. Appl. Phys.* **2012**, *111* (11), 113709.
- (15) Vargas, C.; Zhu, Y.; Coletti, G.; Chan, C.; Payne, D.; Jensen, M.; Hameiri, Z. Recombination Parameters of Lifetime-Limiting Carrier-Induced Defects in Multicrystalline Silicon for Solar Cells. *Appl. Phys. Lett.* **2017**, *110* (9), 092106.
- (16) Diez, S.; Rein, S.; Roth, T.; Glunz, S. W. Cobalt Related Defect Levels in Silicon Analyzed by Temperature- and Injection-Dependent Lifetime Spectroscopy. *J. Appl. Phys.* **2007**, *101* (3), 033710.
- (17) Rosenits, P.; Roth, T.; Glunz, S. W.; Beljakowa, S. Determining the Defect Parameters of the Deep Aluminum-Related Defect Center in Silicon. *Appl. Phys. Lett.* **2007**, *91* (12), 122109.
- (18) Zhu, Y. *Advanced Characterization of Defects in Silicon Wafers and Solar Cells*; UNSW, 2019.
- (19) Morishige, A. E.; Jensen, M. A.; Needleman, D. B.; Nakayashiki, K.; Hofstetter, J.; Li, T. A.; Buonassisi, T. Lifetime Spectroscopy Investigation of Light-Induced Degradation in p-Type Multicrystalline Silicon PERC. *IEEE Journal of Photovoltaics* **2016**, *6* (6), 1466–1472.
- (20) Zhu, Y.; Gia, Q. T. L.; Juhl, M. K.; Coletti, G.; Hameiri, Z. Application of the Newton–Raphson Method to Lifetime Spectroscopy for Extraction of Defect Parameters. *IEEE Journal of Photovoltaics* **2017**, *7* (4), 1092–1097.
- (21) Bernardini, S.; Naeiland, T. U.; Coletti, G.; Bertoni, M. I. Defect Parameters Contour Mapping: A Powerful Tool for Lifetime Spectroscopy Data Analysis. *physica status solidi (b)* **2018**, *255* (8), 1800082.
- (22) Buratti, Y.; Le Gia, Q. T.; Dick, J.; Zhu, Y.; Hameiri, Z. Extracting Bulk Defect Parameters in Silicon Wafers Using Machine Learning Models. *npj Computational Materials* **2020**, *6* (1), 1–8.
- (23) Buratti, Y.; Dick, J.; Gia, Q. L.; Hameiri, Z. A Machine Learning Approach to Defect Parameters Extraction: Using Random Forests to Inverse the Shockley-Read-Hall Equation. In *46th IEEE Photovoltaic Specialist Conference*; 2019; pp 3070–3073.
- (24) Grau-Luque, E.; Guc, M.; Becerril-Romero, I.; Izquierdo-Roca, V.; Pérez-Rodríguez, A.; Bolt, P.; Van den Bruele, F.; Ruhle, U. Thickness Evaluation of AlOx Barrier Layers for Encapsulation of Flexible PV Modules in Industrial Environments by Normal Reflectance and Machine Learning. *Progress in Photovoltaics: Research and Applications* **2021**, DOI: 10.1002/pip.3478.
- (25) Zhu, H.; Yan, W.; Liu, Y.; Hu, D.; Tu, Y.; Huang, Z.; Tan, X. Design Investigation on 100 Mm-Thickness Thin Silicon PERC Solar Cells with Assistance of Machine Learning. *Materials Science in Semiconductor Processing* **2022**, *137*, 106198.
- (26) Wagner-Mohnsen, H.; Altermatt, P. P. A Combined Numerical Modeling and Machine Learning Approach for Optimization of Mass-Produced Industrial Solar Cells. *IEEE Journal of Photovoltaics* **2020**, *10* (5), 1441–1447.
- (27) Wagner-Mohnsen, H.; Esefeller, S.; Klöter, B.; Mitchell, B.; Schinke, C.; Bredemeier, D.; Jäger, P.; Brendel, R. Combining Numerical Simulations, Machine Learning and Genetic Algorithms for Optimizing a POCl₃ Diffusion Process. In *2021 IEEE 48th Photovoltaic Specialists Conference (PVSC)*; 2021; pp 0528–0531.
- (28) Ren, Z.; Oviedo, F.; Xue, H.; Thway, M.; Zhang, K.; Li, N.; Dario, J.; Layurova, M.; Wang, Y.; Tian, S.; Heumueller, T.; Birgersson, E.; Lin, F.; Sun, S.; Peters, I. M.; Stangl, R.; Brabec, C. J.; Buonassisi, T. Physics-Guided Characterization and Optimization of Solar Cells Using Surrogate Machine Learning Model. In *46th IEEE Photovoltaic Specialist Conference*; 2019; p 5.
- (29) Ren, Z.; Oviedo, F.; Thway, M.; Tian, S. I. P.; Wang, Y.; Xue, H.; Dario Perea, J.; Layurova, M.; Heumueller, T.; Birgersson, E.; Aberle, A. G.; Brabec, C. J.; Stangl, R.; Li, Q.; Sun, S.; Lin, F.; Peters, I. M.; Buonassisi, T. Embedding Physics Domain Knowledge into a Bayesian Network Enables Layer-by-Layer Process Innovation for Photovoltaics. *npj Computational Materials* **2020**, *6* (1), 1–9.
- (30) Olikh, O.; Lozitsky, O.; Zavhorodnii, O. Estimation for Iron Contamination in Si Solar Cell by Ideality Factor: Deep Neural Network Approach. *Progress in Photovoltaics: Research and Applications* **2022**, 1–13.
- (31) Kurchin, R. C.; Poindexter, J. R.; Vähäniemi, V.; Savin, H.; del Cañizo, C.; Buonassisi, T. How Much Physics Is in a Current–Voltage Curve? Inferring Defect Properties from Photovoltaic Device Measurements. *IEEE Journal of Photovoltaics* **2020**, *10* (6), 1532–1537.
- (32) Buratti, Y.; Sowmya, A.; Evans, R.; Trupke, T.; Hameiri, Z. Half and Full Solar Cell Efficiency Binning by Deep Learning on Electroluminescence Images. *Progress in Photovoltaics: Research and Applications* **2022**, *30* (3), 276–287.
- (33) Demant, M.; Virtue, P.; Kovvali, A.; Yu, S. X.; Rein, S. Learning Quality Rating of As-Cut Mc-Si Wafers via Convolutional Regression Networks. *IEEE Journal of Photovoltaics* **2019**, *9*, 1–9.
- (34) Goodfellow, I.; Bengio, Y.; Courville, A. *Deep Learning*; MIT Press, 2016.
- (35) Deitsch, S.; Christlein, V.; Berger, S.; Buerhop-Lutz, C.; Maier, A.; Gallwitz, F.; Riess, C. Automatic Classification of Defective Photovoltaic Module Cells in Electroluminescence Images. *Sol. Energy* **2019**, *185*, 455–468.
- (36) Tang, W.; Yang, Q.; Xiong, K.; Yan, W. Deep Learning Based Automatic Defect Identification of Photovoltaic Module Using Electroluminescence Images. *Sol. Energy* **2020**, *201*, 453–460.
- (37) Demirci, M. Y.; Beşli, N.; Güümüşü, A. Efficient Deep Feature Extraction and Classification for Identifying Defective Photovoltaic Module Cells in Electroluminescence Images. *Expert Systems with Applications* **2021**, *175*, 114810.
- (38) Zhang, X.; Hao, Y.; Shangguan, H.; Zhang, P.; Wang, A. Detection of Surface Defects on Solar Cells by Fusing Multi-Channel Convolution Neural Networks. *Infrared Physics & Technology* **2020**, *108*, 103334.
- (39) Tian, S.; Li, W.; Li, S.; Tian, G.; Sun, L.; Ning, X. Image Defect Detection and Segmentation Algorithm of Solar Cell Based on Convolutional Neural Network. In *2021 6th International Conference on Intelligent Computing and Signal Processing (ICSP)*; 2021; pp 154–157.
- (40) Su, B.; Chen, H.; Chen, P.; Bian, G.; Liu, K.; Liu, W. Deep Learning-Based Solar-Cell Manufacturing Defect Detection with Complementary Attention Network. *IEEE Transactions on Industrial Informatics* **2021**, *17* (6), 4084–4095.
- (41) Trupke, T.; Bardos, R. A.; Schubert, M. C.; Warta, W. Photoluminescence Imaging of Silicon Wafers. *Appl. Phys. Lett.* **2006**, *89* (4), 044107.
- (42) Fuyuki, T.; Kondo, H.; Yamazaki, T.; Takahashi, Y.; Uraoka, Y. Photographic Surveying of Minority Carrier Diffusion Length in Polycrystalline Silicon Solar Cells by Electroluminescence. *Appl. Phys. Lett.* **2005**, *86* (26), 262108.
- (43) Rougieroux, F. E.; Sun, C.; Macdonald, D. Determining the Charge States and Capture Mechanisms of Defects in Silicon through Accurate Recombination Analyses: A Review. *Sol. Energy Mater. Sol. Cells* **2018**, *187*, 263–272.

- (44) Green, M. A. Intrinsic Concentration, Effective Densities of States, and Effective Mass in Silicon. *J. Appl. Phys.* **1990**, *67* (6), 2944–2954.
- (45) Couderc, R.; Amara, M.; Lemiti, M. Reassessment of the Intrinsic Carrier Density Temperature Dependence in Crystalline Silicon. *J. Appl. Phys.* **2014**, *115* (9), 093705.
- (46) Yan, D.; Cuevas, A. Empirical Determination of the Energy Band Gap Narrowing in Highly Doped N+ Silicon. *J. Appl. Phys.* **2013**, *114* (4), 044508.
- (47) Henry, C. H.; Lang, D. V. Nonradiative Capture and Recombination by Multiphonon Emission in GaAs and GaP. *Phys. Rev. B* **1977**, *15* (2), 989–1016.
- (48) Lax, M. Cascade Capture of Electrons in Solids. *Phys. Rev.* **1960**, *119* (5), 1502–1523.
- (49) Altermatt, P. P.; Geelhaar, F.; Trupke, T.; Dai, X.; Neisser, A.; Daub, E. Injection Dependence of Spontaneous Radiative Recombination in C-Si: Experiment, Theoretical Analysis, and Simulation. In *NUSOD '05. Proceedings of the 5th International Conference on Numerical Simulation of Optoelectronic Devices*; 2005; pp 47–48. DOI: [10.1109/NUSOD.2005.1518128](https://doi.org/10.1109/NUSOD.2005.1518128).
- (50) Virtanen, P.; Gommers, R.; Oliphant, T. E.; Haberland, M.; Reddy, T.; Cournapeau, D.; Burovski, E.; Peterson, P.; Weckesser, W.; Bright, J.; van der Walt, S. J.; Brett, M.; Wilson, J.; Millman, K. J.; Mayorov, N.; Nelson, A. R. J.; Jones, E.; Kern, R.; Larson, E.; Carey, C. J.; Polat, L.; Feng, Y.; Moore, E. W.; VanderPlas, J.; Laxalde, D.; Perktold, J.; Cimrman, R.; Henriksen, I.; Quintero, E. A.; Harris, C. R.; Archibald, A. M.; Ribeiro, A. H.; Pedregosa, F.; van Mulbregt, P.; et al. SciPy 1.0 Contributors. SciPy 1.0: Fundamental Algorithms for Scientific Computing in Python. *Nat. Methods* **2020**, *17*, 261–272.
- (51) Simonyan, K.; Zisserman, A. Very Deep Convolutional Networks for Large-Scale Image Recognition. *arXiv:1409.1556 [cs]* **2014**, DOI: [10.48550/arXiv.1409.1556](https://doi.org/10.48550/arXiv.1409.1556).
- (52) Breiman, L. Random Forests. *Machine Learning* **2001**, *45* (1), 5–32.
- (53) Glantz, S. A.; Slinker, B. K. *Primer of Applied Regression and Analysis of Variance*; McGraw-Hill : New York (N.Y.), 1990.
- (54) Fawcett, T. An Introduction to ROC Analysis. *Pattern Recognition Letters* **2006**, *27* (8), 861–874.
- (55) Pedregosa, F.; Varoquaux, G.; Gramfort, A.; Michel, V.; Thirion, B.; Grisel, O.; Blondel, M.; Prettenhofer, P.; Weiss, R.; Dubourg, V.; Vanderplas, J.; Passos, A.; Cournapeau, D. Scikit-Learn: Machine Learning in Python. *Journal of Machine Learning Research* **2011**, *12*, 2825–2830.
- (56) Paszke, A.; Gross, S.; Massa, F.; Lerer, A.; Bradbury, J.; Chanan, G.; Killeen, T.; Lin, Z.; Gimelshein, N.; Antiga, L.; Desmaison, A.; Kopf, A.; Yang, E.; DeVito, Z.; Raison, M.; Tejani, A.; Chilamkurthy, S.; Steiner, B.; Fang, L.; Bai, J.; Chintala, S. PyTorch: An Imperative Style, High-Performance Deep Learning Library. In *Advances in Neural Information Processing Systems*; Wallach, H., Larochelle, H., Beygelzimer, A., Alché-Buc, F., Fox, E., Garnett, R., Eds.; Curran Associates, Inc., 2019; pp 8026–8037.

■ NOTE ADDED AFTER ASAP PUBLICATION

This paper published online October 19, 2022, with an error in equation 5. The correct paper was reposted on October 20, 2022.

□ Recommended by ACS

Experimental Establishment of Phase Diagrams Guided by Uncertainty Sampling: An Application to the Deposition of Zn–Sn–P Films by Molecular Beam Epitaxy

Ryoji Katsume, Yoshitaro Nose, et al.

APRIL 24, 2020

ACS MATERIALS LETTERS

READ ▾

Data-Driven Optimization and Experimental Validation for the Lab-Scale Mono-Like Silicon Ingot Growth by Directional Solidification

Xin Liu, Noritaka Usami, et al.

FEBRUARY 17, 2022

ACS OMEGA

READ ▾

Deep Learning-Based Prediction of Fabrication-Process-Induced Structural Variations in Nanophotonic Devices

Dusan Gostimirovic, Yuri Grinberg, et al.

JULY 20, 2022

ACS PHOTONICS

READ ▾

Colorless Polyamide–Imide Films with Enhanced Thermal and Dimensional Stability and Their Application in Flexible OLED Devices

Yuan-Yuan Liu, Da-Yong Wu, et al.

SEPTEMBER 30, 2022

ACS APPLIED POLYMER MATERIALS

READ ▾

Get More Suggestions >